



Novel urea assisted hydrothermal synthesis of hierarchical BiVO₄/Bi₂O₂CO₃ nanocomposites with enhanced visible-light photocatalytic activity

Puttaswamy Madhusudan^a, Jingrun Ran^a, Jun Zhang^a, Jiaguo Yu^{a,*}, Gang Liu^{b,**}

^a State Key Laboratory of Advanced Technology for Materials Synthesis and Processing, Wuhan University of Technology, Wuhan 430070, PR China

^b National Center for Nanoscience and Technology, Beijing 100190, PR China

ARTICLE INFO

Article history:

Received 4 May 2011

Received in revised form 9 September 2011

Accepted 12 September 2011

Available online 18 September 2011

Keywords:

Hierarchical structures

BiVO₄/Bi₂O₂CO₃

Nanosheet

Visible light

Photocatalysis

ABSTRACT

A novel hydrothermal approach is developed for the first time to synthesize hierarchical BiVO₄/Bi₂O₂CO₃ nanocomposites with reactive crystalline facets using urea as a morphology mediator. The as-prepared samples were characterized by X-ray diffraction, scanning electron microscopy, transmission electron microscopy, X-ray photoelectron spectroscopy, Raman spectroscopy, Fourier transform infrared spectroscopy, N₂ absorption–desorption isotherms and UV–visible diffuse reflectance spectroscopy. The photocatalytic activity of the as-prepared samples was evaluated towards degradation of Rhodamine B (RhB) by visible-light. Our results indicate that both physical parameters and associated photocatalytic activity of BiVO₄/Bi₂O₂CO₃ nanocomposites can be tuned by urea concentration and reaction time in the synthesis process. With increasing urea concentration, the specific surface area, pore volume and average pore size increase. Compared to BiVO₄ and Bi₂O₂CO₃ bulk counterpart, BiVO₄/Bi₂O₂CO₃ nanocomposites show enhanced photocatalytic degradation activity of RhB. The mechanisms for the formation of BiVO₄/Bi₂O₂CO₃ nanocomposites and enhanced photoreactivity are discussed.

© 2011 Elsevier B.V. All rights reserved.

1. Introduction

Over the past decades, considerable efforts have been made to design and synthesize nanostructures for water-splitting and organic pollutant degradation under UV and visible-light irradiation [1–6]. Ever since Fujishima and Honda reported water-splitting by TiO₂, there has been significant attention towards the preparation of low-dimensional nanomaterials (e.g., nanosheets) in micro- and nano-regime with well-defined reactive facets, which could be useful in splitting water and decomposition of organic pollutants [7]. For example, theoretical and experimental studies on the photocatalytic activity of anatase TiO₂ showed that the {001} facets are much more reactive than {101} facets [8–10]. Very recently, TiO₂ nanomaterials with highly reactive {001} facets and excellent photoreactivity were successfully prepared in our laboratory [11–14]. Nevertheless, TiO₂ is only active under UV excitation due to its large band gap. Therefore, developing novel solar-driven photocatalysts is highly desirable [15–18]. Indeed, there are a lot of visible-light responsive photocatalysts such as CdS, CdSe, Bi₂WO₆, BiVO₄, Bi₂S₃, CdIn₂S₄, Fe₂O₃, etc. have been reported in literatures [19,20].

In recent years, bismuth-based nanostructured materials are receiving great attention due to their potential applications in semiconductors, catalysts and biomedicine. As an important multicomponent semiconductor, bismuth vanadate (BiVO₄) has relatively narrow bandgap with a wide range of applications in ferroelectrics, photochemical solar cells, ionic conductivity, photocatalytic evolution of O₂, and photodegradation of organic pollutants [21]. Since crystalline bismuth vanadates were reported [22], many synthesis approaches have been developed for the fabrication of monoclinic BiVO₄ crystals, such as solid state reaction, co-precipitation, hydrothermal treatment, aqueous process, sonochemistry and metalorganic decomposition [23–27]. Among these approaches, hydrothermal methods show great promises due to its simplicity in preparing monoclinic BiVO₄ with perfect crystallinity and controllable morphologies in an environmental benign way. Given that the size, shape and phase of BiVO₄ are crucial in determining the photocatalytic properties, a variety of crystal architectures has been fabricated. For example, Xie and co-workers [28] reported synthesis of ellipsoidal m-BiVO₄ nanostructures by oleic acid assisted solvothermal process. Zhang et al. [29] synthesized monoclinic BiVO₄ nanosheets using SDBS surfactant as a morphology-directing template. Kudo and Yu [30] prepared highly crystalline monoclinic BiVO₄ with polyhedral and rod-like morphologies via a hydrothermal process. Zhou et al. prepared single-crystalline monoclinic BiVO₄ microtubes by employing a reflux method [31]. Meng et al. reported monoclinic BiVO₄

* Corresponding author. Tel.: +86 27 87871029; fax: +86 27 87879468.

** Corresponding author. Tel.: +86 10 82545613; fax: +86 10 62656765.

E-mail addresses: jiaguoyu@yahoo.com (J. Yu), liug@nanocr.cn (G. Liu).

single-crystallites with different morphologies using a triblock copolymer P123 assisted hydrothermal method [32]. Very recently, Ye and Xi reported synthesis of monoclinic BiVO_4 nanoplates with exposed $\{001\}$ facets and remarkable visible-light photocatalytic activity [33]. However, most architectures were synthesized in the presence of surfactants, which not only add the costs but make it difficult to scale up production. Therefore, it is of great significance to synthesize BiVO_4 nanostructure with desirable morphology in the absence of surfactants.

In addition, bismuth-containing materials with particular layered structures could present unique photocatalytic properties under visible-light. For instance, aurivillius structured $\text{Bi}_2\text{O}_2\text{CO}_3$ constitutes of layered structure with alternative stacking of $(\text{Bi}_2\text{O}_2)^{2+}$ sheets interleaved by CO_3^{2-} groups. Furthermore, the internal layered structure of aurivillius structured $\text{Bi}_2\text{O}_2\text{CO}_3$ could guide the lower growth rate along (001) axis compared to that along other axes, and thus form 2D morphologies like nanosheets. The highly anisotropic internal structure of $\text{Bi}_2\text{O}_2\text{CO}_3$ could facilitate the formation of sheet-like morphology with particular exposed facets potentially unique and useful in photocatalysis. To the best of our knowledge, $\text{Bi}_2\text{O}_2\text{CO}_3$ is primarily used in medicine and microelectrode [34–37], and less attention has been directed towards its photocatalytic applications [38,39].

In this study, we report for the first time the synthesis of hierarchical $\text{BiVO}_4/\text{Bi}_2\text{O}_2\text{CO}_3$ nanocomposites by a novel low-temperature template-free hydrothermal approach. Compared to BiVO_4 bulk counterparts, the as-synthesized hierarchical $\text{BiVO}_4/\text{Bi}_2\text{O}_2\text{CO}_3$ nanocomposites with exposed high reactive facets display enhanced photodegradation towards Rhodamine B (RhB) by visible-light.

2. Experimental details

2.1. Sample preparation

All the chemicals are of analytical reagent grade and were used as received from Shanghai Chemical Reagent Factory of China without further purification. Distilled water was used in all our experiments. In a typical synthesis, 2.33 g of Bi_2O_3 and 0.58 g of NH_4VO_3 were dissolved in 15 ml of 4.0 M HNO_3 aqueous solution separately and stirred for 30 min at room temperature to form a clear solution. Then these two solutions were mixed together to obtain stable yellow clear solution. A certain amount of urea was added to the above solution and further stirred for 30 min. The amount of urea added was from 0, 6, 12 to 20 g and the corresponding samples were labeled as U0, U6, U12 and U20, respectively. The resulting precursor suspension was loaded into a Teflon-lined stainless steel autoclave with a capacity of 50 ml and maintained at 180°C for 24 h, and subsequently cooled to room temperature naturally. The precipitate was then collected by centrifugation, washed with distilled water and ethanol for several times to remove ions and un-reacted urea and then dried in a vacuum oven at 60°C for 10 h. For comparison, pure $\text{Bi}_2\text{O}_2\text{CO}_3$ nanosheets were also prepared according to the method reported by Huang and co-workers [38].

2.2. Characterization

The powder X-ray diffraction (XRD) patterns of as-prepared samples were obtained on an X-ray diffractometer (type HZG41B-PC) using monochromatized $\text{Cu K}\alpha$ (0.15418 nm) at a scan rate (2θ) of 0.05°s^{-1} . The accelerating voltage and the applied current were 40 kV and 80 mA, respectively. The average crystallite sizes were calculated according to Scherrer formula ($d = 0.89\lambda / \beta \cos \theta$, where d , λ , β and θ are crystallite size, $\text{Cu K}\alpha$ wavelength,

full width at half maximum intensity and Bragg's diffraction angle, respectively). Scanning electron microscopy (SEM) images were recorded by a field emission scanning electron microscopy (JEOL, Japan) at an accelerating voltage of 5 kV. Transmission electron microscopy (TEM) and high-resolution transmission electron microscopy (HRTEM) analyses were conducted using JEM-2100F electron microscopy (JEOL, Japan) operating at 200 kV. The Brunauer–Emmett–Teller (BET) specific surface area (S_{BET}) of the powders was analysed by nitrogen adsorption in a Micromeritics ASAP 2020 nitrogen adsorption apparatus (USA). All the as-prepared samples were degassed at 180°C prior to nitrogen adsorption measurements. The BET surface area was determined by a multipoint BET method using the adsorption data in the relative pressure (P/P_0) range of 0.05–0.3. A desorption isotherm was used to determine the pore size distribution via the Barret–Joyner–Halender (BJH) method, assuming a cylindrical pore model [40]. The nitrogen adsorption volume at the relative pressure (P/P_0) of 0.994 was used to determine the pore volume and average pore size. The X-ray photoelectron spectroscopy (XPS) measurement was performed in an ultrahigh vacuum VG ESCALAB 210 electron spectrometer using $\text{Mg K}\alpha$ (1253.6 eV) radiation source (operating at 200 W) of a twin anode in the constant analyzer energy mode with a pass energy of 30 eV. All the binding energies were referenced to the adventitious C1s line at 284.8 eV as the internal standard. Raman spectra were recorded at room temperature using a micro-Raman spectrometer (Renishaw InVia) in the back-scattering geometry with a 514.5 nm Ar^+ laser as an excitation source. The Fourier transform infrared spectroscopy (FTIR) of the samples was recorded on IRAffinity-1 FTIR spectrometer (Shimadzu, Japan) at a resolution of 4 cm^{-1} . UV–visible absorbance spectra of composite powders were obtained for the dry-pressed disk samples with a UV–visible spectrophotometer (UV-2550, Shimadzu, Japan) using BaSO_4 as a standard.

2.3. Photocatalytic activity

The photocatalytic activity of the as-prepared samples was evaluated towards photodegradation of RhB aqueous solutions at ambient temperature. In details, 0.1 g of the as-prepared catalyst powders was dispersed in a 20 ml of RhB ($2 \times 10^{-5} \text{ mol L}^{-1}$) aqueous solutions in a 90 mm culture dish. Prior to irradiation, the suspensions were kept in the dark for 30 min to reach an adsorption–desorption equilibrium. A 350 W Xenon lamp (Shanghai Lansheng Electronic Co., China) with a 420 nm cutoff filter positioned 25 cm above the dish was used as a visible light source to trigger the photocatalytic reaction. The integrated visible-light intensity on the surface of the reaction solution was measured with a visible-light radiometer (Model: FZ-A, made in Photoelectric Instrument Factory of Beijing Normal University, China). The concentration of pollutant was determined by an UV–visible spectrophotometer (UV-2550, Shimadzu, Japan). At an interval of 15 min, the reaction solution was sampled to record the intensity change of absorption peak at 553 nm.

3. Results and discussion

3.1. Phase structures and morphology

The crystalline structures of the as-prepared samples were examined by X-ray diffraction. Fig. 1 shows the XRD patterns of the as-prepared samples obtained under various conditions. As shown in Fig. 1, $\text{BiVO}_4/\text{Bi}_2\text{O}_2\text{CO}_3$ nanocomposite photocatalysts are well crystallized. The diffraction pattern of sample U0 is indexed with standard data of monoclinic scheelite BiVO_4 structure (JCPDS card No. 14-0688) and no other impurities were detected, indicating

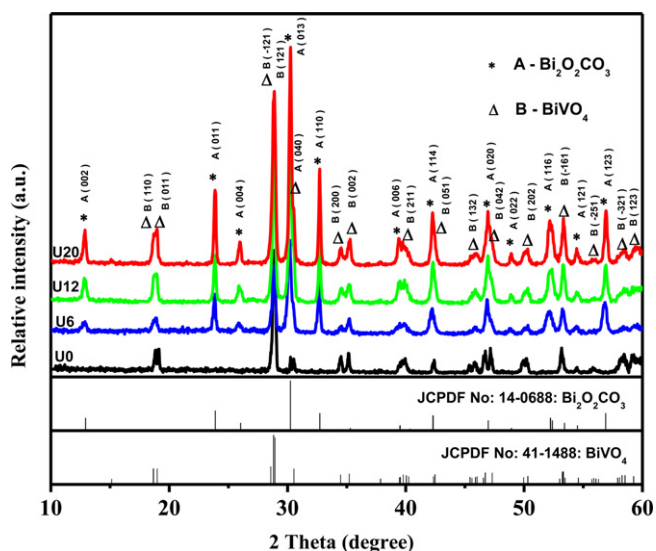


Fig. 1. XRD patterns of nanocomposites products obtained in the presence of different amounts of urea. 0 g (U0), 6 g (U6), 12 g (U12) and 20 g (U20) along with standard XRD patterns of BiVO_4 and $\text{Bi}_2\text{O}_2\text{CO}_3$.

that a pure monoclinic BiVO_4 phase was obtained. When urea was used as precursor in the samples (denoted as U6, U12 and U20), diffraction patterns of tetragonal $\text{Bi}_2\text{O}_2\text{CO}_3$ structures (JCPDS card No. 41-1488) are indexed along with the standard XRD patterns of monoclinic BiVO_4 . Furthermore, the diffraction peaks of nanocomposite are sharp and intense, indicating the highly crystalline nature

of the composites. Also, the intensity of diffraction peaks of BiVO_4 and $\text{Bi}_2\text{O}_2\text{CO}_3$ is increased gradually with increasing urea concentration. In addition, it is noteworthy to mention that the intensity ratio of the (1 1 0) peak to the (0 1 3) peak of $\text{Bi}_2\text{O}_2\text{CO}_3$ is 0.587 in our experiment, much higher than the standard value (0.386), which suggests the anisotropic growth of $\text{Bi}_2\text{O}_2\text{CO}_3$ along the (1 1 0) plane [39].

The morphology and microstructure of sample U20 were revealed by SEM, TEM and HRTEM. Fig. 2a shows typical SEM image of hierarchical $\text{BiVO}_4/\text{Bi}_2\text{O}_2\text{CO}_3$ nanocomposites, which are composed of 2D nanosheets with 50–75 nm in thickness and an average 700–800 nm in width. According to the above observations, the as-prepared composite are stacked layer-by-layer with well-developed $\text{Bi}_2\text{O}_2\text{CO}_3$ nanosheet structure enclosed with BiVO_4 nanoparticles. The well-developed sheet-like structure and morphology of the products were also confirmed by a high-magnification TEM image. Fig. 2b shows a typical HRTEM image of $\text{BiVO}_4/\text{Bi}_2\text{O}_2\text{CO}_3$ nanocomposite, and the inset of this figure shows the low-resolution TEM image. The clear lattice fringe indicates the high-crystallinity of nanocomposites. The fringe spacing of 0.255 nm agrees with the spacing of the (0 2 0) lattice plane of monoclinic BiVO_4 . Furthermore, the lattice spacing of $\text{Bi}_2\text{O}_2\text{CO}_3$ nanosheet is measured to be 0.271 nm, which corresponds to (1 1 0) crystal plane of $\text{Bi}_2\text{O}_2\text{CO}_3$ [41]. Both the HRTEM and XRD results reveal that the nanosheets grew along the (1 1 0) direction. However, $\text{Bi}_2\text{O}_2\text{CO}_3$ nanosheets are highly sensitive and melt upon electron beam irradiation. TEM image of individual nanosheet is shown in Fig. 2c and the subsequent nanosheet after the beam exposure is shown in Fig. 2d. After 5 min of intensive electron beam irradiation, the $\text{Bi}_2\text{O}_2\text{CO}_3$ nanosheets are transformed into

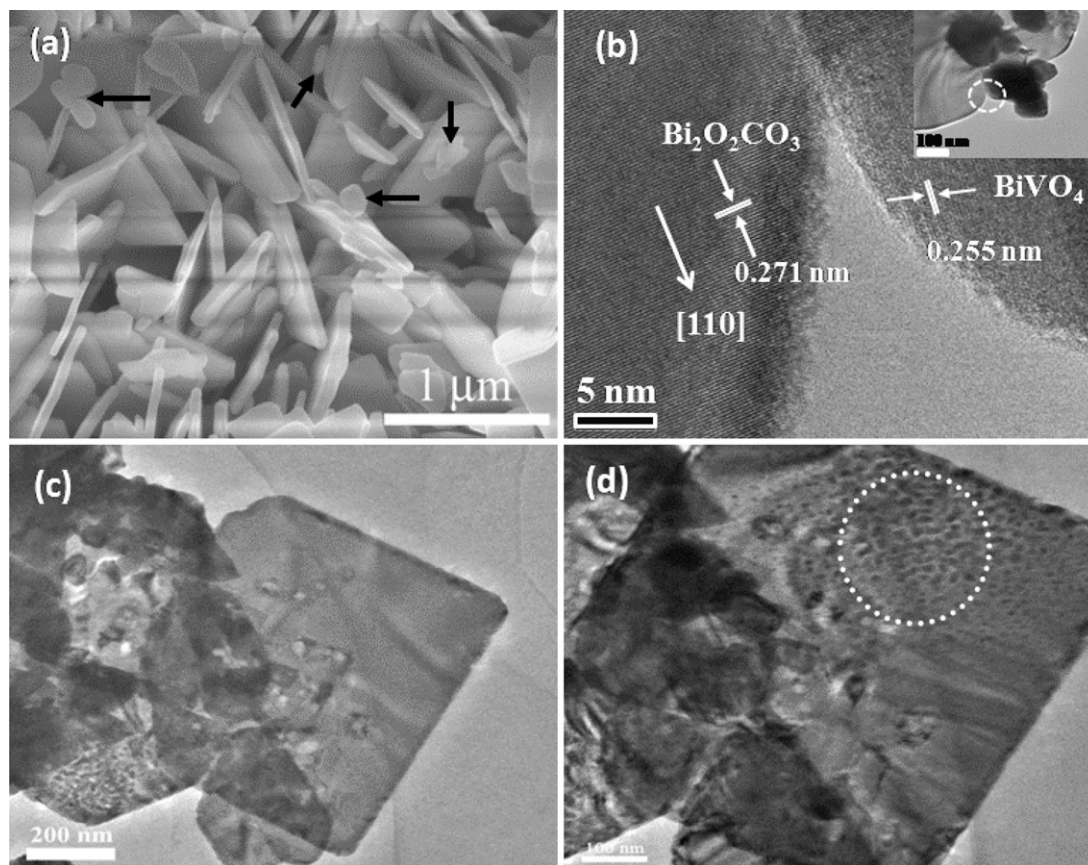


Fig. 2. (a) SEM image of the $\text{BiVO}_4/\text{Bi}_2\text{O}_2\text{CO}_3$ composite (U20) where BiVO_4 particles are marked with arrow heads, (b) HRTEM image of $\text{BiVO}_4/\text{Bi}_2\text{O}_2\text{CO}_3$ nanocomposite showing the lattice fringes (inset in b shows TEM image of $\text{BiVO}_4/\text{Bi}_2\text{O}_2\text{CO}_3$ nanocomposite), (c) TEM image of $\text{Bi}_2\text{O}_2\text{CO}_3$ nanosheets before beam irradiation and (d) $\text{Bi}_2\text{O}_2\text{CO}_3$ nanosheets after 5 min of electron beam irradiation.

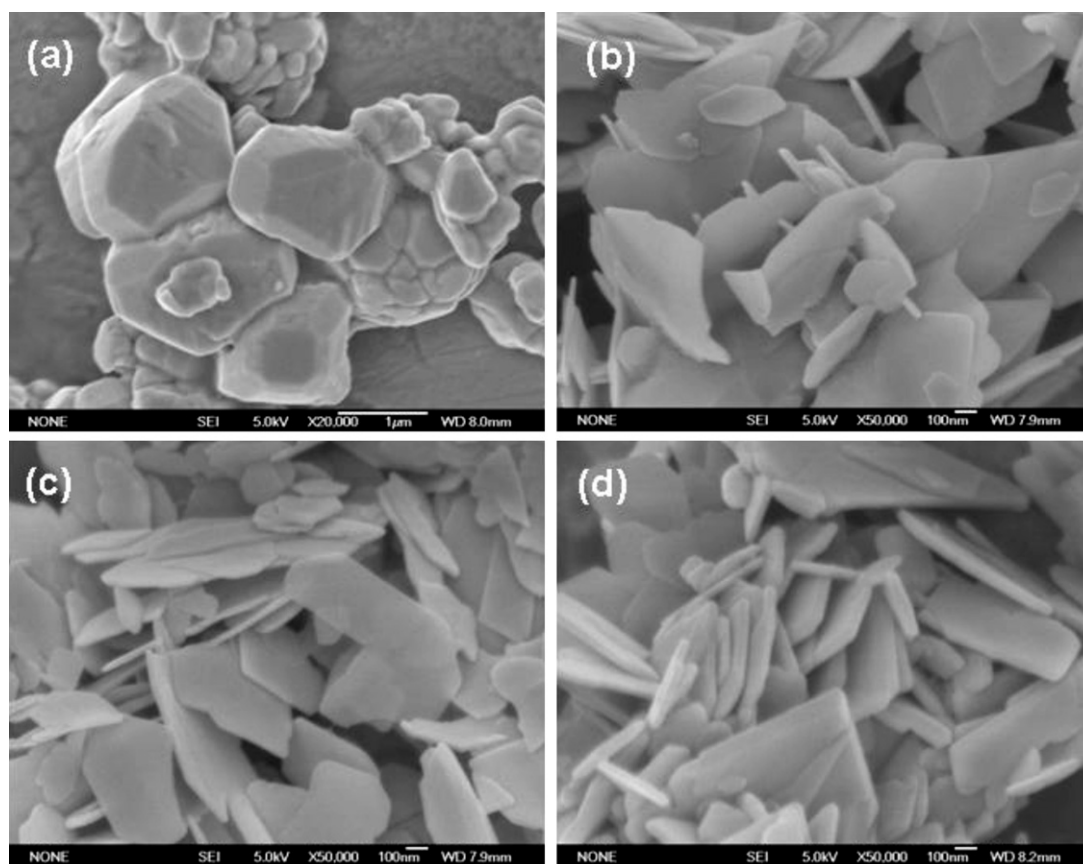


Fig. 3. SEM images of the samples prepared at varying urea content (a) 0, (b) 6, (c) 12 and (d) 20 g.

small granular particles marked as a circle. This result was also reported by many other researchers [42–45]. Thus, the beam sensitivity makes the analysis of electron diffraction slightly difficult. In summary, analyses by XRD, SEM, TEM and HRTEM have demonstrated that $\text{Bi}_2\text{O}_2\text{CO}_3$ nanosheets with exposed (001) facets were obtained.

3.2. Formation mechanism

To understand the formation mechanism of such a nanosheets-based hierarchical structure, experiments under different conditions were conducted and it was observed that the synthesis parameters are crucial in controlling the morphology of the products. Fig. 3 shows the SEM images of the samples obtained at different urea concentration. As shown in Fig. 3a, without urea monoclinic scheelite BiVO_4 bulk crystals with 1–2 μm in size were obtained. This observation can be qualitatively explained in the context that in the absence of urea, BiVO_4 nucleates first and grows as bulk crystals. Interestingly, as shown in Fig. 3b, sheet-like nanostructures with a thickness of about 20–30 nm are formed with 6 g urea added. A closer observation of these sheets reveals that they are attached to each other. Furthermore, when synthesis was performed with 12 g of urea, well-developed nanosheets with 30–50 nm in thickness are observed in Fig. 3c. In addition, these nanosheets are stacked over each other. When the amount of urea is increased from 12 to 20 g, as shown in Fig. 3d, well-developed nanosheets are formed with the edge thickness of about 50–75 nm and length of around 700–800 nm.

On the basis of the above morphology and phase structure analyses, it is believed that during the hydrothermal process urea was thermally decomposed. The reaction is under kinetic control and results in the formation of precipitating agents like ammonia and

carbon dioxide, which maintain the stability of pH value in the solution [46,47]. Such urea hydrolysis reactions are extensively used for the preparation of layer-structured materials [48]. In our experiments, possible reaction pathways are summarized in Eqs. (1)–(5). As temperature increases, urea decomposes to generate CO_2 , which is dissolved in water and hydrolyzed to form CO_3^{2-} ion. Meanwhile, Bi^{3+} ion reacts with nitric acid solution to form $\text{Bi}(\text{NO}_3)_3$, which strongly hydrolyzes to produce slightly soluble BiONO_3 .

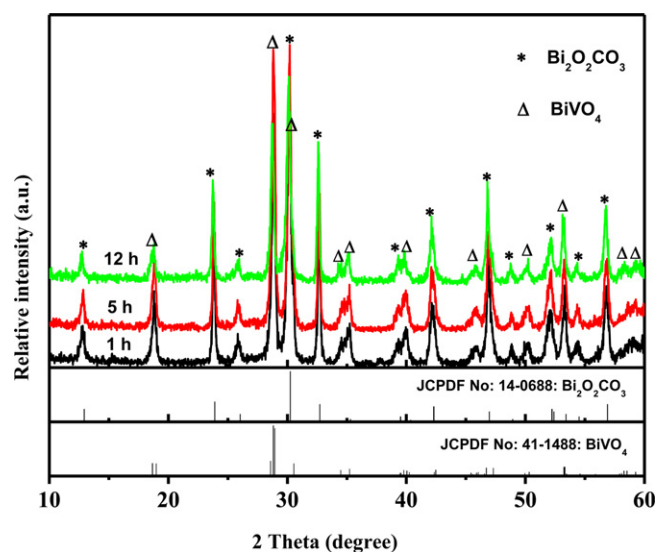


Fig. 4. XRD patterns of sample U20 prepared at different hydrothermal reaction time intervals (a) 1, (b) 5 and (c) 12 h.

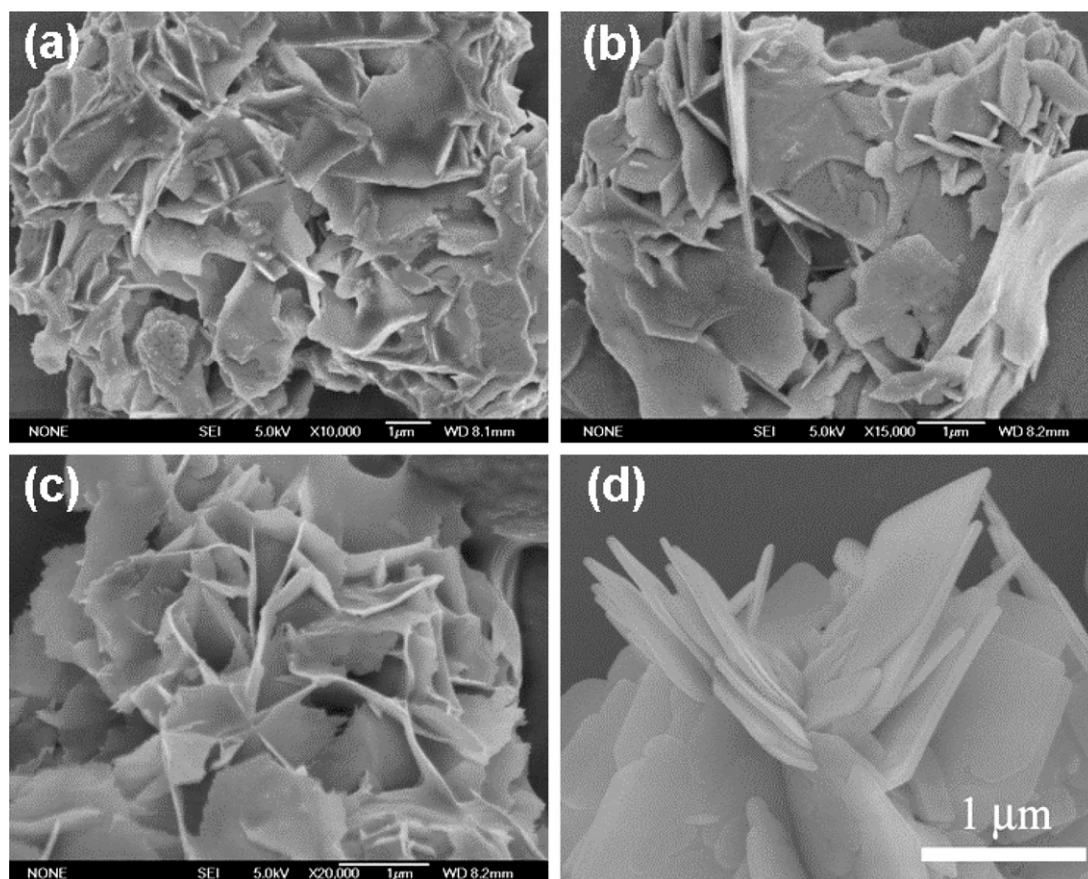
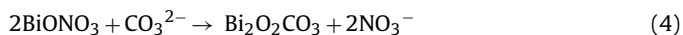
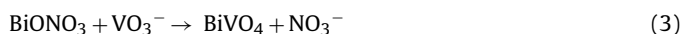
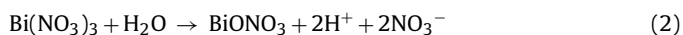
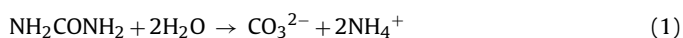


Fig. 5. SEM images of sample U20 prepared at different reaction time interval (a) 1, (b) 5, (c) 12 and (d) 24 h.

Then, the produced CO_3^{2-} , VO_3^- and BiONO_3 species reacts simultaneously to form hierarchical $\text{BiVO}_4/\text{Bi}_2\text{O}_2\text{CO}_3$ nanocomposites and the chemical reactions involved in the process can be formulated as follows: [39,49]



The above results indicate that urea supplies CO_3^{2-} in the reaction and benefits the formation of nanosheets. Furthermore, it is believed that urea also acts as a precursor and provides suitable growth conditions for highly anisotropic nanosheets.

To investigate the growth process, systematic time-dependent experiments were carried out and intermediate products were analysed at different stages. Notably, it can be observed that $\text{BiVO}_4/\text{Bi}_2\text{O}_2\text{CO}_3$ composites are formed within 1 h of hydrothermal reactions. As shown in Fig. 4, the intensities of XRD peaks steadily increase with hydrothermal time, indicating the growth of nanosheets. The corresponding SEM images show irregular shaped nanosheets with the size ranging from 2 to 5 μm (Fig. 5a). At 5 h, less ordered agglomerated sheets are produced (Fig. 5b). As the reaction time is prolonged to 12 h, it can be seen that the products are dominated by flower-like multilayered thin sheets with 1–2 μm in length (Fig. 5c). Moreover, when the hydrothermal reaction time was extended to 24 h, well-developed nanosheets are formed (Fig. 5d) and their corresponding XRD peaks show relative higher intensities. According to the above SEM observations,

we can thus assume that initially irregular nanosheets are precipitated and structurally converted into more stable nanosheets with increasing hydrothermal reaction time. Furthermore, it can be inferred from the above results that the morphology as well as thickness of the nanosheets could be easily controlled by varying urea concentration and hydrothermal reaction time.

3.3. XPS analysis

XPS analysis was conducted to elucidate the surface composition and chemical state of samples U0 and U20. Fig. 6 shows XPS

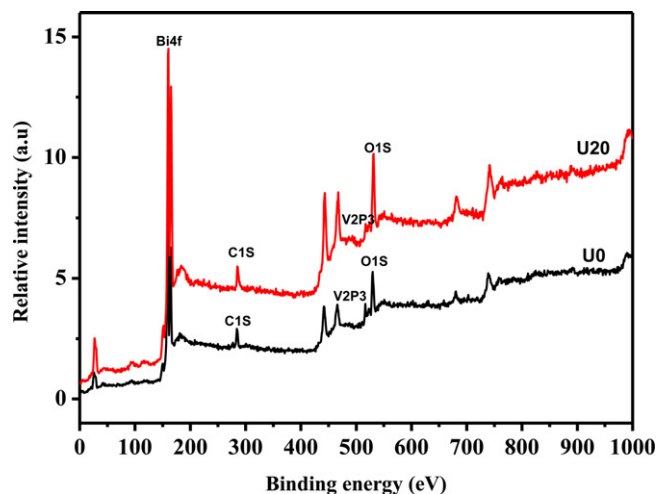


Fig. 6. Typical XPS survey spectra of samples U0 and U20.

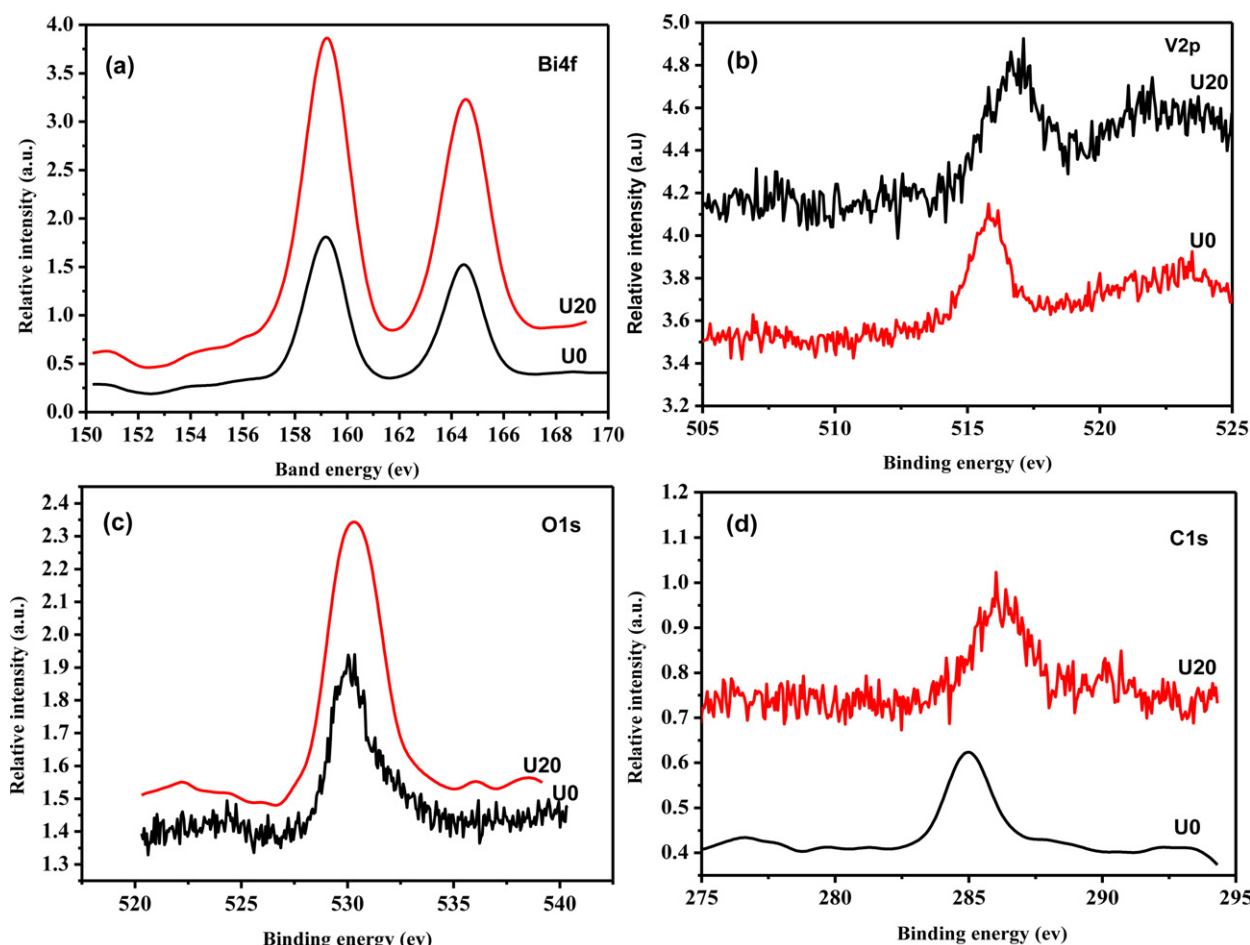


Fig. 7. High-resolution XPS spectra of samples U0 and U20, (a) Bi 4f region XPS spectra, (b) V 2p region XPS spectra, (c) O 1s region XPS spectra and (d) C 1s region XPS spectra.

survey spectra of pure BiVO_4 bulk sample (U0) and $\text{BiVO}_4/\text{Bi}_2\text{O}_3\text{CO}_3$ nanocomposites (U20). Fig. 7a displays two strong symmetrical characteristic peaks for spin-orbit split of Bi 4f peaks located at ca. 159.2 and 165.0 eV, consistent with the Bi $4f_{7/2}$ and Bi $4f_{5/2}$ signals induced by Bi^{3+} ions [50]. Fig. 7b and c illustrate the V $2p_{3/2}$ and O 1s core-level XPS spectra of U0 and U20, respectively. The V $2p_{3/2}$ signals at 516.9 and 516.6 eV are attributed to V^{5+} species on the surface of as-prepared samples. The O 1s peak displays slight asymmetry, indicating that different oxygen species are present in the surface region, such as the lattice oxygen (530 eV) and the chemisorbed OH^- and CO_3^{2-} species on the U20 surfaces (530.3 eV). The C 1s peak (Fig. 7d) at 285 eV observed in BiVO_4 bulk sample is due to adventitious carbon. However, for sample U20 the C 1s peak shifts to higher binding energy, probably due to the presence of CO_3^{2-} species in the composites. Compared to those of sample U0, the binding energies for O 1s and Bi $4f_{7/2}$ of sample U20 increase. Contrarily, the binding energy for V $2p_{3/2}$ dramatically decreases. In other words, the amount of V^{5+} species decreases with increasing chemisorbed CO_3^{2-} species, implying the formation of layered nanocomposites.

3.4. BET surface areas and pore size distributions

The nitrogen adsorption–desorption isotherms of as-prepared samples are presented in Fig. 8. The sample U0 displays type III (Brunauer–Deming–Teller (BDDT) classification) isotherm, which characteristically indicates that weak interaction take place between N_2 molecules and the samples. The isotherm corresponding to U20 sample is of type IV and has two

hysteresis loops at relative pressure between 0.2 and 1.0, indicating bimodal pore-size distributions in the mesoporous and macroporous regions. The shapes of the hysteresis loops are different from each other. At a low relative pressure, between 0.2 and 0.8, the shape of the hysteresis loop is of type H2, suggesting the existence of ink-bottle pores with narrow necks and wider bodies (ink-bottle pores) [40]. At relatively high pressure ranging from 0.8 to 1.0, the shape of the hysteresis loop is of type H3, indicating the presence of slit-shaped pores [50,51]. Furthermore, the composite sample U20 shows high absorption at high relative pressure (P/P_0) range (approaching 1.0), indicating the formation of large mesopores and macropores [52–54]. In fact, the bimodal pore-size distribution is ascribed to two different pores: fine intra-aggregated pores formed between the BiVO_4 particles and large inter-aggregated pores formed between nanosheets. This bimodal pore-size distribution is further confirmed by its corresponding pore-size distributions (see inset of Fig. 8), which are calculated from desorption branch of the nitrogen isotherms by the BJH method. It shows small mesopores with peak pore diameter about 2.3 nm, medium mesopores at narrow range of 3.5–4.3 nm with a maximum pore diameter of about 3.8 nm and large mesopores and macropores at wide range of 10–100 nm with a peak pore diameter of about 60 nm, further confirming the formation of mesopores and macropores [55,56]. These results demonstrate the formation of hierarchically nanoporous structures in U20 sample on a multilength scale. Table 1 shows BET surface area, pore volume and average pore size of U0, U6, U12 and U20 samples. In general, the nanocomposite sample U20 shows larger average pore size, BET surface area and pore volume than BiVO_4 bulk crystals. This result is ascribed to the formation of

Table 1
Physical properties of as-prepared samples.

Sample no.	Urea content (g)	S_{BET} (m^2/g)	Pore volume (cm^3/g)	Pore size (nm)	Crystallite size ^a (nm) (BiVO_4)	Crystallite size ^a (nm) ($\text{Bi}_2\text{O}_3\text{CO}_3$)
U0	0	0.14	0.0002	6.89	36.5	0
U6	6	1.7	0.0035	7.01	34.2	53.6
U12	12	3.3	0.0057	7.04	32.8	52.6
U20	20	3.8	0.0072	7.56	30.0	67.0

^a Average crystallite size of BiVO_4 and $\text{Bi}_2\text{O}_3\text{CO}_3$ was determined by XRD using Scherrer equation from the (1 2 1) diffraction peak of BiVO_4 and the (1 1 0) diffraction peak of $\text{Bi}_2\text{O}_3\text{CO}_3$, respectively.

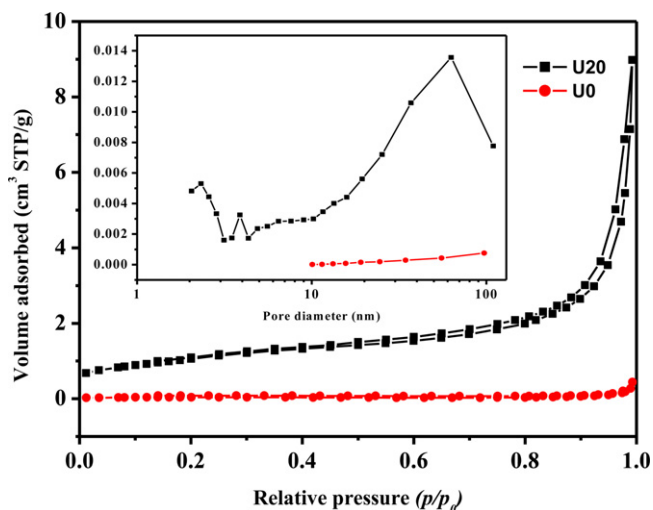


Fig. 8. Nitrogen adsorption-desorption isotherms and the corresponding pore-size distribution curves (inset) of samples U0 and U20.

nanosheet structures which are stacked over each other. In general, the porous structures are expected to be useful in the photocatalytic process by offering efficient transport pathways to reactants and the products, in addition to facilitating the absorption of pollutants for degradation [57].

3.5. Raman and FTIR spectroscopy analysis

Fig. 9 shows Raman spectra of as-prepared samples. The intense Raman band at ca. 832 cm^{-1} is attributed to the stretching modes of V–O bond, and the bands at 330 and 373 cm^{-1} are assigned to asymmetric and symmetric deformation modes of VO_4^{3-} tetrahedron, respectively. In sample U20, the intensities of two bands at 330 and 373 cm^{-1} decrease, suggesting the weak deformation of

VO_4^{3-} tetrahedron. Furthermore, the intensity of stretching modes of V–O bond at ca. 832 cm^{-1} decreases and shifts to low frequency in comparison with other samples, probably due to the relationship between the Raman stretching frequencies and the metal-oxygen bond length in the local structure corresponding to longer bond length.

To investigate the chemical composition and chemical bonding of composites, FTIR was carried out and the corresponding spectra are shown in Fig. 10. Two bands at about 3389 and 1730 cm^{-1} can be attributed to the stretching and deformation vibration of the O–H groups of chemisorbed and/or physisorbed water molecules. The band at 548 cm^{-1} is assigned to the metal–oxygen bonds. The bands at 700 – 910 cm^{-1} are assigned to ν_1 (VO_4) and ν_3 (VO_4). The spectra of U6, U12 and U20 show intensive peak at 1351 cm^{-1} , which are assigned to the ν_3 mode of the CO_3^{2-} group while the peaks at 1065 and 844 cm^{-1} are ascribed to the ν_1 and ν_2 modes of the CO_3^{2-} group, respectively [58]. In addition, the peak at 2373 cm^{-1} derived from the vibration of the CO_3^{2-} group, is also observed in all samples. The CO_3^{2-} vibration band in U0 could be attributed to trapped or adsorbed CO_2 impurities from the atmosphere.

3.6. UV–vis diffuse reflectance spectroscopy

It is well-known that the optical absorption of a semiconductor is closely related to its electronic structure. The UV–vis diffuse reflectance spectra and corresponding photos of samples U0, U20 and pure $\text{Bi}_2\text{O}_3\text{CO}_3$ nanosheets are shown in Fig. 11 and the samples U0 and U20 display strong absorption in the UV–visible region from 200 to 550 nm . The steep absorption edge at 546 nm of the bulk BiVO_4 sample (U0) spectrum indicates that the visible-light absorption is due to the intrinsic band-gap transition. As can be seen, $\text{Bi}_2\text{O}_3\text{CO}_3$ sample has an absorption edge at about 365 nm . However, the spectrum of sample U20 shows two absorption edges, suggesting that this sample contains two semiconductors of BiVO_4

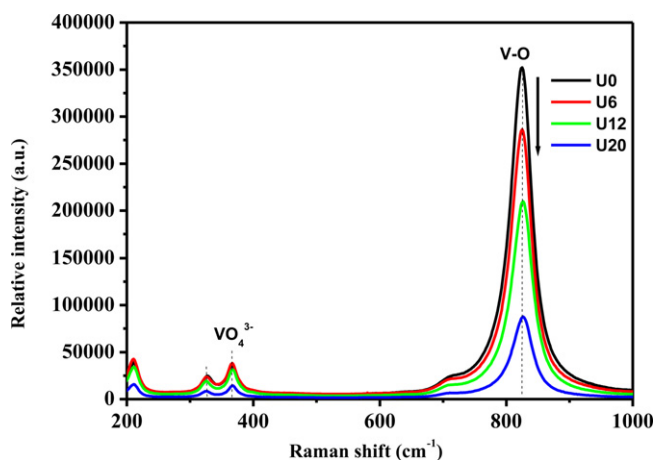


Fig. 9. Raman spectra of samples U0, U6, U12 and U20.

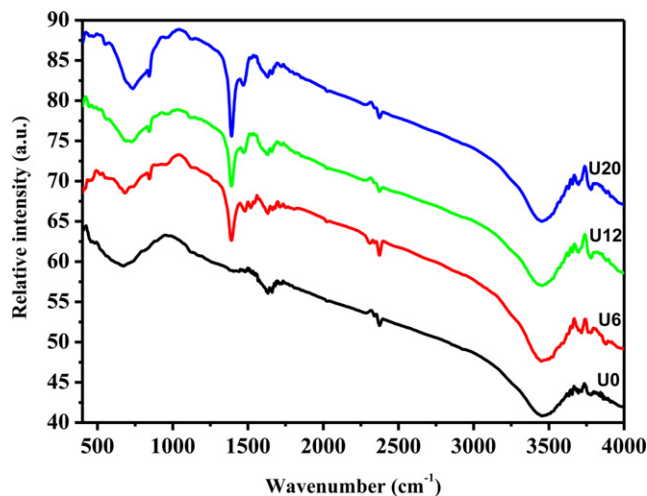


Fig. 10. FTIR spectra of samples U0, U6, U12 and U20.

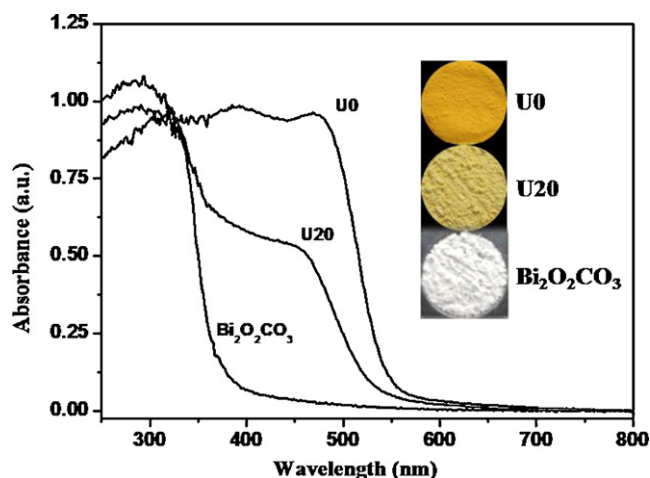


Fig. 11. UV-vis absorption spectra of BiVO₄ (U0) and BiVO₄/Bi₂O₂CO₃ nanocomposite (U20) compared with pure Bi₂O₂CO₃ nanosheets. The inset shows color variation of samples U0, U20 and Bi₂O₂CO₃.

and Bi₂O₂CO₃. The absorbance edge at about 430 nm is ascribed to Bi₂O₂CO₃, while BiVO₄ shows a sharp edge at 502 nm which shows a significant blue shift compared with U0 resulting probably from quantum-size effects [59]. This is confirmed by decreasing crystallite size of BiVO₄ in U20 compared to U0 (see Table 1).

The Kubelka-Munk function based on the diffuse reflectance spectra is employed to determine the band gap [60]. For the indirect band gap semiconductor, the relation between the absorption coefficient (α) and photon energy ($h\nu$) can be written as

$$\alpha = \frac{B_{\text{ind}}(h\nu - E_g)^2}{h\nu} \quad (6)$$

where B_{ind} is absorption constants for indirect transitions. α can be determined from the scattering and reflectance spectra according to Kubelka-Munk theory [61]. The indirect band gaps estimated from the Kubelka-Munk function are ca. 2.47 and 2.90 eV for respective BiVO₄ and Bi₂O₂CO₃ in sample U20, consistent with previous results [31,38,62]. Compared with the bandgap of bulk BiVO₄ nanostructures, the bandgap of nanocomposites slightly increases, presumably due to quantum-size effects resulting from the nano-sized building blocks among the nanosheet structures. In addition, these data demonstrate that the electronic structures of composites can be controlled by the reaction conditions in the hydrothermal synthesis.

3.7. Photocatalytic activity

The as-prepared hierarchical BiVO₄/Bi₂O₂CO₃ nanocomposites are expected to exhibit high photocatalytic efficiency. We examined photocatalytic degradation of RhB dye aqueous solution under visible-light irradiation. Fig. 12a shows the temporal change of absorption spectra of dye solutions exposed to visible light as a function of time in the presence of sample U20. With increasing photodegradation time, the peak intensity of RhB at around 553 nm decreases, indicating the destruction of RhB structure over the as-prepared samples. Decolorization occurs after 60 min of irradiation and no new absorption bands emerge in either the visible or the ultraviolet regions, suggesting that the chromophoric structure of the dye is completely broken down. The variation of RhB concentration (C/C_0) with irradiation time over different photocatalysts is depicted in Fig. 12b. For comparison, direct photolysis of dye solution is performed under the same conditions without photocatalysts. Only 5% of RhB is photolyzed after 60 min irradiation. In contrast, BiVO₄/Bi₂O₂CO₃ nanocomposites display a much higher

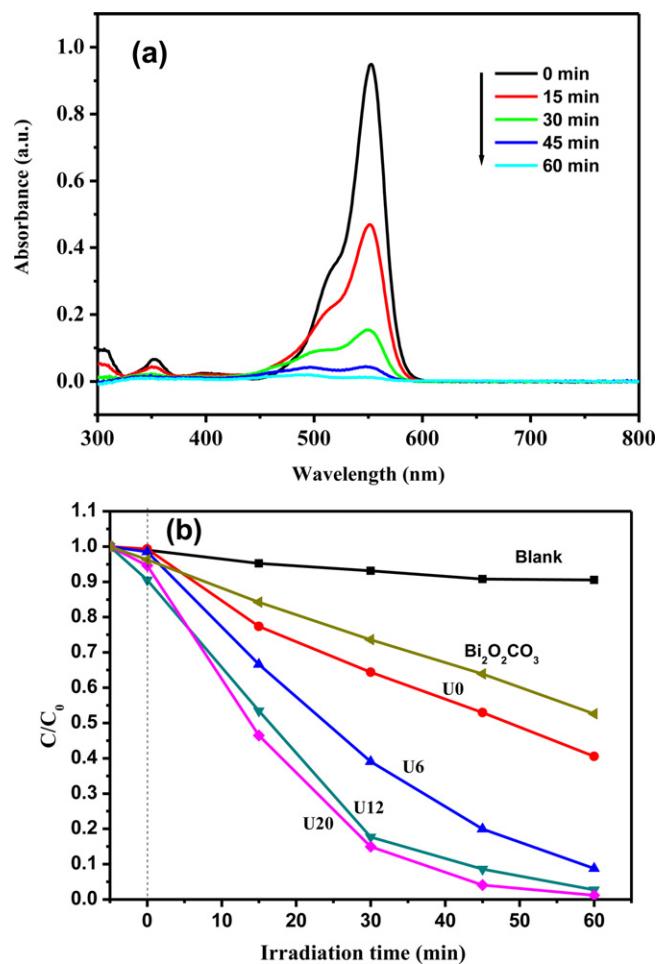


Fig. 12. (a) Absorption changes of RhB aqueous solution in the presence of U20 and (b) comparison of photocatalytic activities of as-prepared samples for the photocatalytic decolorization of RhB in water.

photodegradation rate (97% in 60 min) than bulk BiVO₄ (U0) (54% in 60 min) and Bi₂O₂CO₃ nanosheet (47% in 60 min).

According to the above experimental results, the enhanced photocatalytic activity of hierarchical BiVO₄/Bi₂O₂CO₃ nanocomposites can be attributed to the combined effect of several factors. Firstly, U20 nanocomposites with unique hierarchical nanosheet-like superstructures could facilitate transportation of reactants and products on the photocatalyst surfaces and result in the easy chemical reactions [54]. Secondly, the stacked layered nanosheets allow multiple reflection of light, thus enhancing light harvesting and increasing the quantity of photogenerated electrons and holes. Thirdly, relative large surface area and high crystallinity of nanocomposites may be a key factor in photocatalytic degradation. Finally, the photocatalytic activity of a photocatalyst mainly depends on whether the electron-hole pairs can be effectively separated. It is generally accepted that the migration direction of the photogenerated charge carrier depends on the band edge positions of semiconductors. The photoinduced electron and hole could migrate to the surface to react with the adsorbed reactants. The band edge positions of the as-prepared semiconductors are theoretically predicted using electronegativity concept [63–65]. The conduction band (CB) and valence band (VB) potentials of the semiconductor at the point of zero charge are calculated by the following equation:

$$E_{\text{VB}} = X - E^{\circ} + 0.5E_g \quad (7)$$

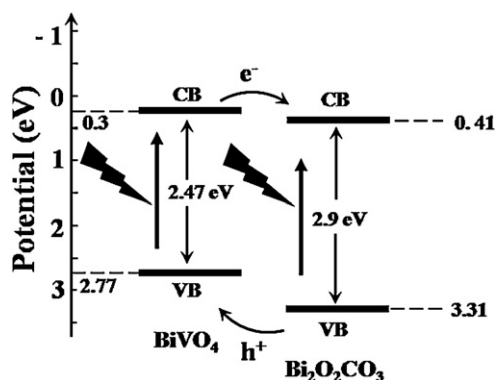


Fig. 13. Schematic illustration for energy bands of BiVO_4 and $\text{Bi}_2\text{O}_2\text{CO}_3$ semiconductors.

where X is the absolute electronegativity of the semiconductor, which is defined as the geometric average of the absolute electronegativity of the constituent atoms, E^e is the energy of free electrons on the hydrogen scale (ca. 4.5 eV), E_{VB} is the VB edge potential and E_g is the band gap of the semiconductor. The conduction band position can be deduced by $E_{\text{CB}} = E_{\text{VB}} - E_g$.

Accordingly, the top of valence band (VB) and bottom of the conduction band (CB) of BiVO_4 are calculated to be 2.77 and 0.3 eV. The VB and CB of $\text{Bi}_2\text{O}_2\text{CO}_3$ are estimated to be 3.31 and 0.41 eV, respectively. Under visible light illumination ($\lambda > 420 \text{ nm}$), $\text{Bi}_2\text{O}_2\text{CO}_3$ could be excited and induced the generation of photoelectrons and holes. According to the schematic diagram in Fig. 13, the conduction band-edge potential of BiVO_4 is more negative than that of $\text{Bi}_2\text{O}_2\text{CO}_3$. Therefore, photo-generated electrons on the surface of BiVO_4 would easily transfer into the conduction band of $\text{Bi}_2\text{O}_2\text{CO}_3$ under the inducement action of the internal electric field, leaving holes in the BiVO_4 valence band. Meanwhile, the photoinduced holes in the valence band of $\text{Bi}_2\text{O}_2\text{CO}_3$ could be transferred to valence band of BiVO_4 . Thus, the photo-generated electrons and holes in the $\text{Bi}_2\text{O}_2\text{CO}_3$ and BiVO_4 could be separated effectively in the $\text{BiVO}_4/\text{Bi}_2\text{O}_2\text{CO}_3$ nanocomposites, and the recombination of electron–hole pairs can be reduced. The separated charge carriers undergo reactions with the reactants adsorbed on the photocatalyst surface and subsequently enhance the photocatalytic activity.

The stability of highly efficient U20 photocatalyst is further evaluated by the recycle experiments. The photodegradation rate of U20 comparatively decreases during the third cycle, which might

be due to the presence of superficial inorganic species and organic adsorbates on the surface of U20. However, as shown in Fig. 14, the photodegradation efficiency of the nanocomposites after ultrasonic cleaning with ethanol and water solutions is found to be significantly improved. Furthermore, photocatalytic efficiency does not show major loss after five recycles and only slight decrease in photodegradation efficiency over time is observed, indicating that the nanocomposites are relatively stable and not photocorroded during the photocatalytic process.

4. Conclusions

In summary, for the first time hierarchical $\text{BiVO}_4/\text{Bi}_2\text{O}_2\text{CO}_3$ nanocomposites with highly exposed reactive $\{001\}$ facets were prepared by a urea-assisted hydrothermal approach. The urea concentration and associated reaction time play a crucial role in determining the morphology, crystallinity, and crystallite size. The higher the urea concentration, the greater the BET specific surface area, pore volume and average pore size are. Compared to bulk BiVO_4 and $\text{Bi}_2\text{O}_2\text{CO}_3$ nanosheets, the as-prepared nanocomposites show enhanced photocatalytic activity for degradation of RhB under visible-light irradiation. Furthermore, the present study motivates us to explore hydrothermal method for the preparation of new nanocomposites with a high percentage of reactive facets, which could be employed not only in photocatalysis, but also in pigment, catalysis, separation technology, biomedical engineering and nanotechnology.

Acknowledgements

This work was partially supported by the National Natural Science Foundation of China (20877061 and 51072154), Natural Science Foundation of Hubei Province (2010CDA078), National Basic Research Program of China (2007CB613302) and Self-determined and Innovative Research Funds of SKLWUT.

References

- [1] M.R. Hoffmann, S.T. Martin, W.Y. Choi, D.W. Bahnemann, *Chem. Rev.* 95 (1995) 69.
- [2] J.G. Yu, X.X. Yu, *Environ. Sci. Technol.* 42 (2008) 4902.
- [3] M. Ksibi, S. Rossignol, J.M. Tatibouet, C. Trapalis, *Mater. Lett.* 62 (2008) 4204.
- [4] M. Paulose, H.E. Prakasham, O.K. Varghese, L. Peng, K.C. Popat, G.K. Mor, T.A. Desai, C.A. Grimes, *J. Phys. Chem. C* 111 (2007) 14992.
- [5] J.G. Yu, X.X. Yu, B.B. Huang, X.Y. Zhang, Y. Dai, *Cryst. Growth Des.* 9 (2009) 1474.
- [6] J.G. Yu, J.R. Ran, *Energy Environ. Sci.* 4 (2011) 1364.
- [7] A. Fujishima, K. Honda, *Nature* 37 (1972) 238.
- [8] X.Q. Gong, A.J. Selloni, *Phys. Chem. B* 109 (2005) 19560.
- [9] H.G. Yang, G. Liu, S.Z. Qiao, C.H. Sun, Y.G. Jin, S.C. Smith, J. Zou, H.M. Cheng, G.Q. Lu, *J. Am. Chem. Soc.* 131 (2009) 4078.
- [10] T. Ohno, K. Sarukawa, M. Matsumura, *New J. Chem.* 26 (2002) 1167.
- [11] (a) S.W. Liu, J.G. Yu, M. Jaroniec, *J. Am. Chem. Soc.* 132 (2010) 11914; (b) Q.J. Xiang, J.G. Yu, M. Jaroniec, *Chem. Commun.* 47 (2011) 4532; (c) K.L. Lv, Q.J. Xiang, J.G. Yu, *Appl. Catal. B* 104 (2011) 275.
- [12] J.G. Yu, Q.J. Xiang, J.R. Ran, S. Mann, *CrystEngComm* 12 (2010) 872.
- [13] J.G. Yu, G.P. Dai, Q.J. Xiang, M. Jaroniec, *J. Mater. Chem.* 21 (2011) 1049.
- [14] Q.J. Xiang, J.G. Yu, M. Jaroniec, *Phys. Chem. Chem. Phys.* 13 (2011) 4853.
- [15] H.J. Snaith, L. Schmidt-Mende, *Adv. Mater.* 19 (2007) 3187.
- [16] B. Lim, M.J. Jiang, P.H.C. Camargo, E.C. Cho, J. Tao, X.M. Lu, Y.M. Zhu, Y.N. Xia, *Science* 324 (2009) 1302.
- [17] R. Schloegl, *Nat. Mater.* 7 (2008) 772.
- [18] M. Schurriner, M. Ballauff, Y. Talmon, Y. Kauffmann, J. Thun, M. Moller, J. Breu, *Science* 323 (2009) 617.
- [19] (a) A. McLaren, T. Valdes-Solis, G. Li, S.C. Tsang, *J. Am. Chem. Soc.* 131 (2009) 12540; (b) J.G. Yu, J. Zhang, M. Jaroniec, *Green Chem.* 12 (2010) 1161.
- [20] Y.X. Zhou, H.B. Yao, Q. Zhang, J.Y. Gong, S.J. Liu, S.H. Yu, *Inorg. Chem.* 48 (2009) 1082.
- [21] A. Kudo, H. Kato, I. Tsuji, *Chem. Lett.* 33 (2004) 1534.
- [22] E. Zintl, *L. Varino, DRP Patent* 422947 (1925).
- [23] A.R. Lim, S.H. Choh, M.S. Jang, *J. Phys. Condens. Matter* 7 (1995) 7309.
- [24] Y. Zhao, Y. Xie, X. Zhu, S. Yan, S. Wang, *Chem. Eur. J.* 14 (2008) 1601.
- [25] S. Kohtani, S. Makino, A. Kudo, K. Tokumura, Y. Ishigaki, T. Matsunaga, O. Nikaido, K. Hayakawa, R. Nakagaki, *Chem. Lett.* 7 (2002) 660.

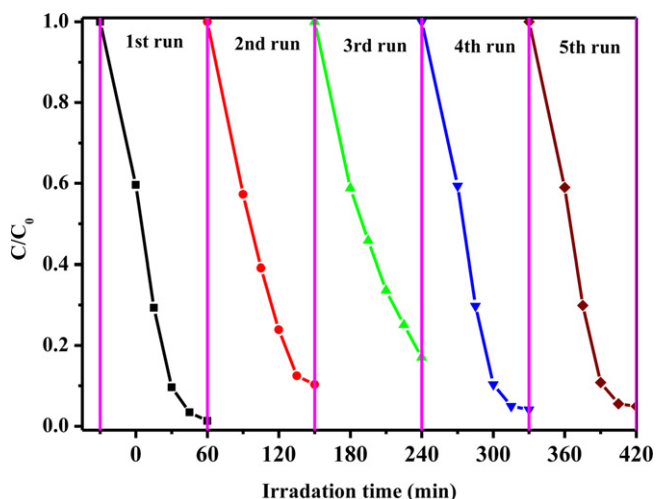


Fig. 14. Cycling runs in the photocatalytic degradation of RhB in the presence of nanocomposites under visible-light.

- [26] Y. Zhou, K. Vuille, A. Heel, B. Probst, R. Kontic, G.R. Patzke, *Appl. Catal. A: Gen.* 375 (2010) 140.
- [27] A. Iwase, H. Kato, A. Kudo, *J. Sol. Energy Eng.* 132 (2010) 021106.
- [28] Y. Sun, C. Wu, R. Long, Y. Cui, S. Zhang, Y. Xie, *Chem. Commun.* 30 (2009) 4542.
- [29] L. Zhang, D. Chen, X. Jiao, *J. Phys. Chem. B* 110 (2006) 2668.
- [30] J.Q. Yu, A. Kudo, *Adv. Funct. Mater.* 16 (2006) 2163.
- [31] L. Zhou, W.Z. Wang, L.S. Zhang, H.L. Xu, W. Zhu, *J. Phys. Chem. C* 111 (2007) 13659.
- [32] X. Meng, L. Zhang, H. Dai, Z. Zhao, R. Zhang, Y. Liu, *Mater. Chem. Phys.* 124 (2011) 59.
- [33] G. Xi, J. Ye, *Chem. Commun.* 46 (2010) 1893.
- [34] J.R. Lambert, P. Midolo, *Aliment. Pharmacol. Ther.* 11 (1997) 27.
- [35] R. Chen, M.H. So, J. Yang, F. Deng, H.Z. Sun, *Chem. Commun.* 21 (2006) 2265.
- [36] G. Cheng, H. Yang, K. Rong, Z. Lu, X. Yu, R.J. Chen, *Solid State Chem.* 183 (2010) 1878.
- [37] P.J. Sadler, H. Li, H. Sun, *Coord. Chem. Rev.* 186 (1999) 689.
- [38] Y. Liu, Z. Wang, B. Huang, K. Yang, X. Zhang, X. Qin, Y. Dai, *Appl. Surf. Sci.* 257 (2010) 172.
- [39] H. Cheng, B. Huang, K. Yang, Z. Wang, X. Qin, X. Zhang, Y. Dai, *ChemPhysChem* 11 (2010) 2167.
- [40] K.S.W. Sing, D.H. Everett, R.A.W. Haul, L. Moscou, R.A. Pierotti, J. Rouquerol, T. Siemieniowska, *Pure Appl. Chem.* 57 (1985) 603.
- [41] Y.Y. Li, J.P. Liu, X.T. Huang, G.Y. Li, *Cryst. Growth Des.* 7 (2007) 1350.
- [42] Z.B. Zhang, D. Gekhman, M.S. Dresselhaus, J.Y. Ying, *Chem. Mater.* 11 (1999) 1659.
- [43] Y. Li, J. Wang, Z. Deng, Y. Wu, X. Sun, D. Yu, P. Yang, *J. Am. Chem. Soc.* 123 (2001) 9904.
- [44] J. Wang, Y. Li, *Adv. Mater.* 15 (2003) 445.
- [45] L. Zhang, D. Chen, X.J. Jiao, *Phys. Chem. B* 110 (2006) 2668.
- [46] M. Yada, A. Ichinose, M. Machida, T. Kijima, *Agrew. Chem. Int. Ed.* 38 (1999) 3506.
- [47] B.T. Holland, P.K. Isbester, C.F. Blanford, E.J. Munson, A. Stein, *J. Am. Chem. Soc.* 119 (1997) 6796.
- [48] S. Vial, J. Ghanbaja, C. Forano, *Chem. Commun.* 3 (2006) 290.
- [49] A. Zhang, J. Zhang, *Appl. Surf. Sci.* 256 (2010) 3224.
- [50] H.Q. Jiang, M. Nagai, K. Kobayashi, *J. Alloys Compd.* 479 (2009) 821.
- [51] H. Xu, H.M. Li, C.D. Wu, J.Y. Chu, Y.S. Yan, H.M. Shu, Z. Gu, *J. Hazard. Mater.* 153 (2008) 877.
- [52] J.G. Yu, J. Zhang, *Dalton Trans.* 39 (2010) 5860.
- [53] J.G. Yu, J.J. Fan, K.L. Lv, *Nanoscale* 2 (2010) 2144.
- [54] X.C. Wang, J.C. Yu, Y.L. Chen, L. Wu, X.Z. Fu, *Environ. Sci. Technol.* 40 (2006) 2369.
- [55] J.G. Yu, B. Wang, *Appl. Catal. B* 94 (2010) 295.
- [56] J.G. Yu, Y.R. Su, B. Cheng, *Adv. Funct. Mater.* 17 (2007) 1984.
- [57] J.G. Yu, J. Zhang, S.W. Liu, *J. Phys. Chem. C* 114 (2010) 13642.
- [58] R. Keuleers, H.O. Desseyn, B. Rousseau, C. Van Alsenoy, *J. Phys. Chem. A* 103 (1999) 4621.
- [59] A. Walsh, Y. Yan, M.N. Huda, M.M. Al-Jassim, S.H. Wei, *Chem. Mater.* 21 (2009) 547.
- [60] N. Serpone, D. Lawless, R. Khairutdinov, *J. Phys. Chem.* 99 (1995) 16646.
- [61] M. Patterson, C.E. Shelden, B.H. Stockton, *Appl. Opt.* 16 (1977) 729.
- [62] M. Shang, W. Wang, S. Sun, J. Ren, L. Zhou, L. Zhang, *J. Phys. Chem. C* 113 (2009) 20228.
- [63] D. Ke, T. Peng, L. Ma, P. Cai, P. Jiang, *Appl. Catal. A* 350 (2008) 111.
- [64] L. Ren, J. Lei, J.B. Wang, M. Qiu, Y. Yu, *Nanotechnology* 20 (2009) 405602.
- [65] Y.I. Kim, S.J. Atherton, E.S. Brigham, T.E. Mallouk, *J. Phys. Chem.* 97 (1993) 11802.